Heliyon 10 (2024) e29255

Contents lists available at ScienceDirect

Heliyon

journal homepage: www.cell.com/heliyon

Research article

Fabrication and synergistically enhanced photocatalytic activity of ternary kaolinite, TiO_2, and Al_2O_3 ($K_{65}T_{30}A_5$) nanocomposite for visible-light-induced degradation of methylene blue and remazol red dye

Nadira Parvin Lata [a], Md. Sheum Hussain [a], Md. Abdulla-Al-Mamun [b,*], Taslim Ur Rashid [a], Sayed Md. Shamsuddin [a]

[a] Department of Applied Chemistry and Chemical Engineering, Faculty of Engineering and Technology, University of Dhaka, Dhaka, 1000, Bangladesh

[b] Institute of Leather Engineering and Technology, University of Dhaka, 44-50 Hazaribagh, Dhaka, 1209, Bangladesh

ARTICLE INFO

Keywords:
Kaolinite
TiO_2
Al_2O_3
Ternary photocatalyst
Photodegradation
Recyclable photocatalysts

ABSTRACT

The ternary photocatalyst ($(Al_2Si_2O_5(OH)_4/TiO_2/Al_2O_3$) composites (where w/w = 65, 30, and 5 wt%) denoted $K_{65}T_{30}A_5$ were successfully synthesized and examined for their efficiency in removing cationic (Methylene Blue, MB) and anionic (Remazol Red, RR) dye from aqueous medium under visible-light irradiation. A series of nanocomposites with varied wt% of kaolinite, TiO_2, and Al_2O_3 were prepared through sonication followed by calcination at 600 °C. X-ray diffraction (XRD) analysis confirmed the crystallinity of the synthesized materials and established their average crystal size to be 83.87 nm. The morphological structure, composite molecule, and surface properties of the resulting $K_{65}T_{30}A_5$ were characterized using FTIR, FE-SEM, and EDS analyses to confirm the successful fabrication of the nanocomposite. FTIR and EDS elemental mapping analyses confirmed the presence of Al, Si, Ti, and O elements in the nanocomposites. The composites exhibited photocatalytic behaviour across the UV–visible spectra, with values varying from the ultraviolet to the visible region with a sharp increase in reflectance at 510 nm. Near-complete degradation of MB (97.66 %) was achieved within 90 min at pH 9 and a 10 mg/L dye concentration, while RR removal reached 90.66 % within 120 min at pH 3.5 and the same dye concentration under visible light irradiation. The catalyst exhibited robust stability, retaining its efficiency by removing 85.09 % of MB and 80.21 % of RR dye after three reuse cycles. The composite catalyst discussed in this study emerges as a promising material for straightforward fabrication techniques, featuring a high percentage of kaolinite and proving to be a cost-effective solution for large-scale water and wastewater treatment processes.

1. Introduction

Wastewater treatment plays a crucial role in preserving water sources and safeguarding the well-being of both aquatic and terrestrial ecosystems. Addressing this challenge is particularly intricate due to the resilience of textile and leather dyes, which are

* Corresponding author.
E-mail address: mamun.ilet@du.ac.bd (Md. Abdulla-Al-Mamun).

https://doi.org/10.1016/j.heliyon.2024.e29255
Received 18 March 2024; Received in revised form 23 March 2024; Accepted 3 April 2024
Available online 7 April 2024

intentionally formulated to withstand exposure to sunlight, soap, oxidizing chemicals, and other environmental conditions. Conventional water treatment methods often prove insufficient in mitigating this issue. Consequently, numerous researchers have explored diverse approaches, including oxidation, membrane filtration, flocculation, coagulation, biological treatment, among others, to effectively remove these persistent dyes from wastewater [1,2]. Recently, photocatalytic degradation has emerged as a more reliable and superior approach for wastewater treatment compared to other methods [3,4].

When a semiconductor absorbs photons with energy greater than its band gap, the photons excite electrons in a semiconductor catalyst, causing them to move from the valence band to the conduction band. This process creates positively charged vacancies, known as holes. In a single-component, such as TiO_2 semiconductor nanoparticles, the efficiency of photocatalysis is relatively low (<5 %), primarily due to a significant portion of the photogenerated charge carriers undergoing recombination [5,6]. To enhance photocatalytic activity, it is crucial to rapidly remove conduction band electrons from TiO_2, preventing their recombination with holes and facilitating successful charge separation.

Heterogeneous photocatalysis utilizing TiO_2 has been a focal point in recent investigations due to the chemical stability, non-toxicity, and potential for the complete degradation of organic compounds in polluted air and wastewater. The band gap (*Eg*) of TiO_2 anatase is approximately ~ 3.2 eV, covering only a limited portion (3–4%) of the solar spectrum [7]. The relatively large band gap has limited its extensive application, especially in indoor settings [8], owing to the ultraviolet spectrum region. Nevertheless, the challenge of isolating TiO_2 from a finely dispersed suspension in dye solutions can be addressed by immobilizing TiO_2 on the surface of a suitable particulate substrate, such as clay [9]. Additionally, clay enhances TiO_2's application by preventing its phase transition from anatase (highly photoactive) to rutile (less photoactive) [10].

Several methods have been proposed to improve the efficiency of photocatalytic processes involving TiO_2 under visible light irradiation. These methods include doping, functionalization of the surface with metal particles, and reduction of particle size to the nanoscale. The disadvantages of a faster electron-hole pair recombination rate and poor organic adsorption properties reduce the photocatalytic activity of TiO_2. Electron-hole recombination rate can be slowed down by doping TiO_2 with metal oxides such as Al_2O_3 or ZnO [11]. Additionally, alumina is employed as a supporting material to enhance the limited organic adsorption properties of TiO_2 [10,12]. Hence, Al_2O_3 is incorporated with kaolinite and TiO_2 in this study to simultaneously address the aforementioned issues. A few binary composite photocatalysts, including TiO_2/kaolinite and TiO_2/Al_2O_3, have been previously reported in the literature [13,14].

However, to the best of our knowledge, the synergistic effect of kaolinite, TiO_2, and Al_2O_3 on the photocatalytic degradation of textile and leather dye has not been reported elsewhere. In this study, we introduce a thermochemical method for producing a novel ternary composite from kaolinite, TiO_2, and Al_2O_3. The ternary composites were chosen for their chemical stability and inherent photocatalytic properties, as evidenced by a low bandgap energy, as reported here. While the composite catalyst in this study demonstrated stability over multiple recycling runs, its recovery posed a challenge. Consequently, the current investigation focused on incorporating kaolinite/TiO_2 into Al_2O_3 to develop a visible light-responsive composite catalyst activated by visible light irradiation. The study employed catalyst synthesis methods with low energy consumption requirements, aligning to advance sustainable technologies. The resulting ternary composite, $K_{65}T_{30}A_5$, demonstrated a remarkable 97.66 % and 90.66 % photocatalytic degradation of Methylene Blue (MB) and Remazol Red (RR) respectively. Langmuir-Hinshelwood isotherm models were applied to the experimental data. The error analysis revealed that the catalytic process was effectively described by the pseudo-first-order and Langmuir-Hinshelwood model.

2. Materials and methods

2.1. Materials

The commercial TiO_2 (mainly anatase grade) and Al_2O_3 (neutral activity I-II) were purchased from MERCK KGaA (Germany). The locally available kaolinite precursors were procured from Bijoypur clay. NaOH pellets, hydrochloric acid (37 %) and buffer solutions (pH 4 and pH 7) were purchased from Active Fine Chemicals Ltd., Dhaka, Bangladesh. Aceton, methanol and ethanol were procured from Merck KGaA, Germany. Ascorbic acid ($C_6H_8O_6$), 2-propanol ($(CH_3)_2CHOH$), and diammonium oxalate monohydrate ($(NH_4)_2C_2O_4{\cdot}H_2O$) were also purchased from Merck KGaA, Germany. Methylene blue (MB) (CAS-122965-43-9) was purchased from Sigma-Aldrich (Merck), and Lab-grade Remazol Red (RR) dye was purchased from local dye suppliers of the textile industry. The stock solutions of MB and RR were prepared using purified deionized water obtained from a UV water purification system, procured from Labtron Equipment Ltd., UK. All chemicals and reagents were utilized without further purification.

2.2. Activation and purification of kaolinite

The purified clay underwent activation through treatment with 2 M hydrochloric acid at room temperature (25 °C) for 48 h, utilizing a mechanical shaker set at 150 rpm. Subsequently, the activated clay was separated from the suspension via centrifugation at 3000 rpm for 10 min. To eliminate residual acid, the clay underwent multiple washing cycles. Following this, the acid-activated clay was subjected to drying in an oven at 100 °C for 10 h. Verification of acid removal was performed using a pH meter.

2.3. Preparation and characterization of ternary photocatalyst nanocomposite

The ternary nanostructured composite was synthesized using a thermochemical method, as illustrated in schematic Fig. 1, outlining the fabrication process for kaolinite/TiO_2/Al_2O_3 nanoparticles. The ternary photocatalyst was derived from a mixture of kaolinite,

TiO_2, and Al_2O_3 in deionized water, blended in various ratios. Homogeneous dispersion of the precursors was achieved through sonication at 50 °C for approximately 60 min. The resulting mixture was then subjected to evaporation in an oven at 80 °C overnight to isolate the solid mass. Subsequently, the dried product underwent grinding to enhance its surface area. The powder was then subjected to incineration in a muffle furnace at 600 °C for 4 h, establishing an optimal thermochemical environment for composite synthesis. Following calcination, the product underwent additional grinding to increase reactivity for effective dye removal operations [11].

X-ray diffraction (XRD) patterns were recorded to examine the phase stage composition of the specimens. The XRD patterns were obtained using an X-ray diffractometer (Ultima IV, Rigaku Corporation, Akishima, Japan) equipped with Cu Kα radiation ($\lambda = 0.154$ nm). The measurements were conducted in a 10°–80° (2θ) scanning range. The instrument operated at 40 mA and 40 kV, with a scanning speed 3° min^{-1} and a scanning step size of 0.02°. Bragg's law was employed to calculate the basal spacing of the crystalline samples. The Field Emission Scanning Electron Microscope (FE-SEM, JSM 7600F, JEOL-Japan) fitted with EDS was utilized for the investigation of the surface morphology and the distribution of particle sizes within the samples. The accelerating voltage used for the FE-SEM measurements was 2.0 kV, while for the EDS analysis, it was set at 15 kV. The sample's functional groups and potential chemical interactions of the composites were measured using Fourier-transform infrared spectroscopy (FT-IR, 8400S, Shimadzu Corporation, Japan) to record their spectra. The FT-IR was employed to identify the functional groups present in the samples within the wave number range of 4000–400 cm^{-1}, with a resolution of 4 cm^{-1} and 30 scans. About 1 mg of the samples underwent grinding with 100 mg of KBr employing an agate mortar, following which pressure was applied to form a pellet from the resulting mixture. Absorption spectra were obtained using a UV–visible spectrophotometer (Shimadzu Corporation, MPS-2000, Kyoto, Japan) with a 1 cm pathlength quartz cuvette. For the investigation of photocatalysts' diffuse reflectance spectra (DRS) in the 190–900 nm range, the UV-3600i Plus UV–Vis–NIR spectrophotometer (Shimadzu Corporation, Japan) was employed. Zeta potential (ζ) measurements were made for point of zero charge (pH_{PZC}) determination using, "Laser Color, LITESIZER 500 series" Anton Paar GmbH, Austria. The formation of hydroxyl radicals (·OH) on the surface of $K_{65}T_{30}A_5$ under visible light irradiation was detected using a photoluminescence technique (Biobase, BK-F96S), with terephthalic acid serving as the probe molecule. Aqueous suspensions containing composite powder were exposed to sunlight for 0, 30, 60, and 90 min. Subsequently, the reaction solution was filtered to measure the photoluminescence intensity. This measurement was conducted within a spectral range of 420 to 470 nm, with 2-hydroxyterephthalic acid, excited wavelength by 320 nm under room temperature.

2.4. Preparation of standard solutions and fixation of the wavelength of maximum absorbance (λ_{max}) and construction of calibration curve

2.4.1. Methylene blue (MB) dye

A concentrated solution of 500 ppm MB was meticulously prepared through dissolution 0.125 g of MB in purified water within a precisely calibrated 250 mL volumetric flask, resulting in a combined volume of 250 mL. Subsequently, a meticulously planned successive dilution steps was meticulously generated from stock solution, meticulously yielding various concentrations (2, 4, 5, 6, 8, 10, 12, 14, and 15 ppm). The meticulously determined λ_{max} (wavelength of maximum absorbance) for MB was meticulously determined, and a meticulously constructed calibration curve illustrating absorbance plotted against concentration was meticulously formed. The meticulously calculated concentration of MB in the water solution was meticulously ascertained at its meticulously identified λ_{max} using a meticulously calibrated UV–visible spectrophotometer.

To establish the λ_{max} of MB, UV–visible spectra of standard solutions containing 5, 10, and 15 ppm concentrations of the dye were meticulously recorded individually using a UV–visible spectrophotometer, covering the wavelength range from 200 to 800 nm. The

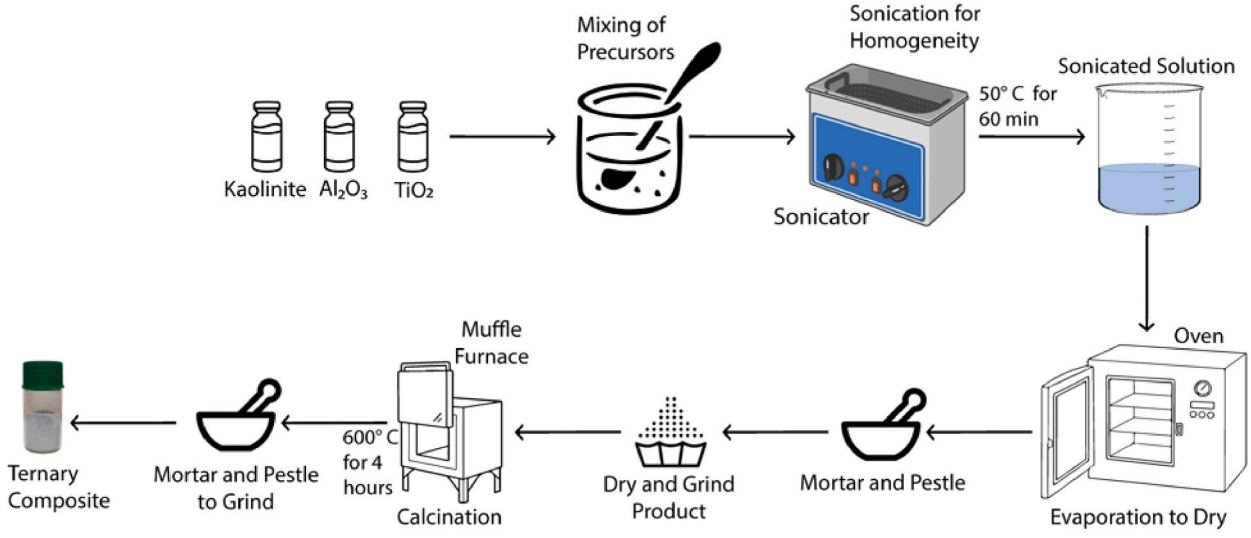

Fig. 1. Pictorial representation of the synthesis process for ternary ($K_{65}T_{30}A_5$) nanocomposites.

wavelength corresponding to the peak absorbance was precisely identified as the λ_{max} of MB. In this meticulous study, the λ_{max} was determined to be 661 nm, and all absorbance measurements of MB solutions were meticulously conducted at this wavelength, as illustrated in Fig. S1(a). The calibration curve (Fig. S1(b)) was meticulously generated by plotting absorbance data values at 661 nm opposing different levels of MB. Subsequently, this meticulously constructed curve was utilized for the precise calculation of unknown concentrations of MB solutions.

2.4.2. Remazol red (RR) dye

A 500 ppm stock solution of RR was prepared by dissolving 0.125 mg of RR in distilled water, and the total volume was adjusted to 250 mL using a 250 mL volumetric flask. Various dilutions were then derived from this stock solution to produce concentrations of 10 ppm, 20 ppm, 30 ppm, 40 ppm, and 50 ppm. The determination of the λ_{max} (wavelength of maximum absorbance) for RR was conducted, followed by the construction of a calibration curve depicting absorbance versus concentration. Subsequently, the concentration of RR in the water solution was assessed at its maximum absorption wavelength using a UV–visible spectrophotometer.

To ascertain the λ_{max}, UV–visible spectra of standard solutions containing 10, 20, 30, 40, and 50 ppm concentrations of the dye were meticulously recorded individually using a UV–visible spectrophotometer across the wavelength range from 200 to 800 nm. The wavelength corresponding to the peak of maximum absorbance was precisely identified and designated as the λ_{max} for RR.

To determine the wavelength of maximum absorbance (λ_{max}) for RR, individual UV–visible spectra were recorded for 10, 20, 30, 40, and 50 ppm standard solutions of the dye. The wavelength corresponding to the maximum absorbance was identified as the λ_{max} for Remazol Red. The λ_{max} was determined to be 519 nm (Fig. S1(c)), and all absorbance measurements of Remazol Red solutions were conducted at this wavelength.

Following this, a calibration curve (Fig. S1(d)) was generated by plotting absorbance data values at 519 nm against a range of RR concentrations. Utilizing this calibration curve, unknown concentrations of RR solutions were accurately calculated, providing a dependable method for determining their concentrations with precision.

2.5. Degradation efficiency of methylene blue (MB) and Remazol Red (RR)

Batch experiments were performed to determine the percentage (%) removal of dye using the nanohybrid particles. 25 mL of MB and RR solutions with various concentrations were separately dispensed into various 100 mL beakers. Subsequently, 5 mg and 10 mg of nanocomposite were added to the beakers containing MB and RR solutions, respectively. A mechanical shaker was employed to agitate the beakers at 120 rpm at room temperature. To optimize the pH of the solutions, 0.1 M NaOH and 0.1 M HCl were introduced. The MB and RR-loaded composites were then subjected to sunlight exposure for degradation. Following this, the composites were isolated from the suspensions by centrifugation at 4000 rpm for 3 min, and the residual concentrations of MB and RR in the solutions were determined by measuring absorbance at 661 nm (λ_{max} of MB) and 519 nm (λ_{max} of RR), respectively.

The percentage removal of dye was calculated using the following formula:

$$\%\ Removal = \frac{(C_o - C_e)}{C_o} \times 100\% \quad (1)$$

where, C_e = the equilibrium concentration of dye (mg/L).; C_o = the initial concentration of dye (mg/L).

2.6. Radical trapping experiments

For investigation of the potential contribution from various photo-generated active species i.e., hole (h^+), superoxide ($\bullet O_2^-$) and hydroxyl radicals ($\bullet$OH) towards the photocatalytic degradation of MB and RR under visible light irradiation respectively, radical trapping experiments were carried out. In this experiment, ammonium oxalate (AO) was introduced as a hole scavenger, 2-propanol as a hydroxyl radical scavenger and ascorbic acid (AA) as a superoxide scavenger [15,16].

Various experiments were conducted to assess the removal of MB and RR under optimized conditions, with the presence of different scavengers. The percentage removal of MB and RR was systematically recorded for each experiment, wherein different 1 mmol/L scavengers were individually introduced. Prior to the addition of the catalyst ($K_{65}T_{30}A_5$), the scavengers were incorporated into the aqueous solution containing MB and RR. As a point of reference, an experiment was conducted without any scavengers. Additionally, a separate experiment without any scavenger (WS) was performed for comparative analysis. The observed decrease in the percentage removal of MB and RR in the presence of specific scavengers indicated that the photocatalytic degradation process was predominantly influenced by the corresponding active species associated with each scavenger.

2.7. Kinetic analysis of methylene blue (MB) and Remazol Red (RR) removal using photocatalysts

To determine the degradation rate of MB and RR, a kinetic analysis was conducted utilizing the Langmuir-Hinshelwood model. The Langmuir-Hinshelwood rate expression is widely acknowledged as the standard model for characterizing the kinetics of heterogeneously catalyzed reactions. This model assumes a single rate-controlling step, providing a comprehensive framework for understanding the dynamics of the degradation process [17].

2.8. Reusability/recyclability of the photocatalysts

The reusability of the synthesized nanocomposite ($K_{65}T_{30}A_5$) was explored over three cycles, maintaining optimized conditions for the degradation of MB (pH: 9, concentration: 10 mg/L, time: 90 min) and Remazol Red (pH: 3.5, concentration: 10 mg/L, time: 90 min), respectively. Following each cycle, the nanocomposite underwent a thorough washing process with plenty of distilled water and filtration to neutralize the pH. Subsequently, the nanocomposite was dried in an oven before being reintroduced for the subsequent cycle, demonstrating its potential for multiple applications.

2.9. TOC analysis

The total Organic Carbon (TOC) of the initial dye solution and the solution irradiated under optimized conditions were measured using a TOC analyzer. Finally, the % reduction in the TOC content of the irradiated sample was measured using the following formula:

$$\%\ \text{TOC reduction} = \frac{\text{TOC}_i - \text{TOC}_f}{\text{TOC}_i} \times 100\% \quad (2)$$

where, TOC_i is the Total Organic Carbon (TOC) content of the initial dye solution in ppm; TOC_f is the Total Organic Carbon (TOC) content of the irradiated solution in ppm.

3. Results and discussion

3.1. Characterization of the ternary photocatalyst

Several studies have investigated the potential of kaolinite/TiO_2/Al_2O_3 ternary photocatalysts for environmental applications. The composites with higher kaolinite content have demonstrated superior photodegradation rates compared to commercial TiO_2 [18]. Similarly, Bai et al. reported enhanced photocatalytic activity in TiO_2/kaolinite composites, with the former attributing this to the presence of anatase TiO_2 crystal grains on the kaolinite surface and the latter to the high specific surface area and heterojunction

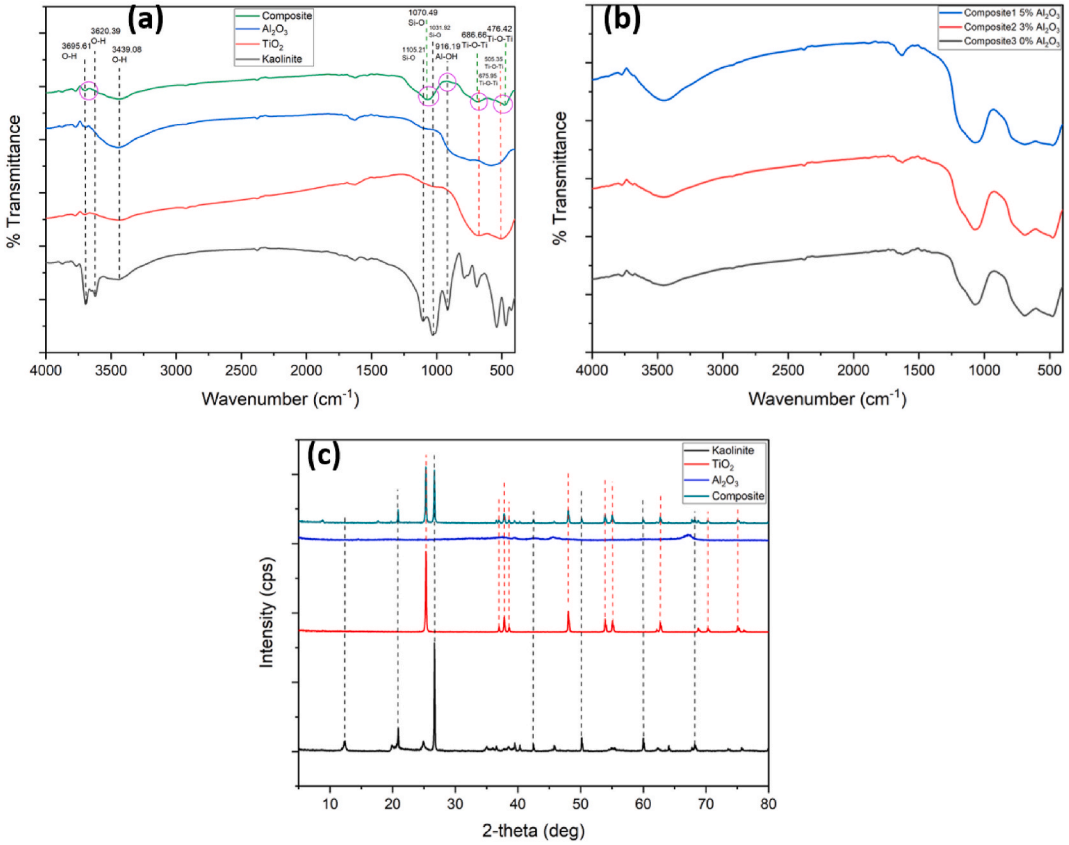

Fig. 2. (a) FTIR spectra of kaolinite, TiO_2, Al_2O_3, and ternary composite ($K_{65}T_{30}A_5$) and (b) FTIR spectra of three distinct ternary composites and (c) XRD patterns for kaolinite, TiO_2, Al_2O_3 and the ternary composite ($K_{65}T_{30}A_5$).

microstructure [19]. Wang et al. further supported these findings, demonstrating that kaolinite facilitated the formation of anatase and enhanced the overall photocatalytic activity of TiO_2 [20].

3.1.1. FTIR analysis

The characteristic peaks of kaolinite and TiO_2 in the FTIR spectra are evident in the ternary composites. Specifically, the Si–O stretching vibration at 1070.49 cm^{-1} confirms the presence of kaolinite. This peak arises from the overlapping of typical peaks of kaolinite at 1105.21 and 1031.92 cm^{-1}. Additionally, two trait peaks of kaolinite at 3695.61 cm^{-1} and 3620.39 cm^{-1}, attributed to the in-phase stretching of the three inner-surface O–H groups and inner O–H stretching bonds, respectively, are significantly diminished within the ternary composites. Furthermore, the typical peak of kaolinite at 916.19 cm^{-1}, corresponding to the Al–OH bond, is entirely absent in the ternary composites. Fig. 2(a) illustrates the geometry and intensity variation of these peaks. The absence of certain kaolinite peaks within ternary composite can be attributed to the high-temperature calcination process. Stretching vibrations of the Ti–*O*–Ti bond at 686.66 cm^{-1} and 476.42 cm^{-1} in ternary composites justify the presence of TiO_2. The peaks are shifted by 10–20 cm^{-1} from the characteristic peaks of TiO_2. See peak assignments in Supporting Information in Table S1.

The FTIR spectra of the three different (Composite-1 contains 65 % kaolinite, 30 % TiO_2, 5 % Al_2O_3; Composite-2 contains 65 % kaolinite, 32 % TiO_2, 3 % Al_2O_3; Composite-3 contains 65 % kaolinite, 35 % TiO_2, 0 % Al_2O_3) composites were observing the spectrum (Fig. 2(b)). It is noticed that the intensity of characteristic peaks for Si–O and Ti–*O*–Ti bonds are reduced and also the peaks are flattened with the increase of Al_2O_3 percentage. This pattern can be explained by the fact that the FT-IR of Al_2O_3 shows a broad band of 500–1000 cm^{-1} [21]. With the increase in the percentage of Al_2O_3, the effects from the band of Al–O bonds increase accordingly. P. Padmaja et al. reported that in the infrared (IR) spectra of Al_2O_3–TiO_2 bulk samples, bands attributed to the stretching vibrations of Al–O bonds in octahedrally coordinated aluminum were observed in the range of 500–750 cm^{-1}. Additionally, in the range of 750–900 cm^{-1}, bands corresponding to vibrations of Al–O bonds in AlO_4 units were present [22].

3.1.2. XRD analysis

The wide-angle X-ray diffraction (XRD) patterns of kaolinite/TiO_2/Al_2O_3 ternary ($K_{65}T_{30}A_5$) photocatalysts and bare kaolinite, TiO_2, Al_2O_3 nanocomposites are shown in Fig. 2(c). The bare kaolinite exhibits well-defined reflections at 2θ values of 12.398°, 20.001°, 20.918°, 24.840°, 26.652°, 50.168°, 60.21°, and 68.30°, which are typically characteristic peaks of kaolinite [23]. Silicon dioxide generally gives peaks at 12.398° and 26.65°, aluminium oxide gives peaks at 50.42°, 60.21°, and 68.30°. The XRD pattern of commercial TiO_2 reveals well-defined reflections at 2θ values of 25.330°, 37.824°, 48.048°, 53.912°, 55.084°, and 62.686° [24]. These peaks correspond to the characteristic tetragonal crystalline structure of anatase-TiO_2, with their corresponding (hkl) planes identified as (101), (004), (200), (105), (211), (204), and (116), respectively. The sharp diffraction patterns observed indicate the small size, high purity, and crystallinity of the TiO_2 sample [25,26]. The XRD pattern of Al_2O_3, as shown in Fig. 2(c), does not reveal any well-defined reflections, indicating the amorphous nature of Al_2O_3. Furthermore, similar XRD patterns with the above-mentioned characteristic peaks were obtained for the synthesized nanocomposite (Fig. 2(c), demonstrating the structural integrity and uninterrupted crystallinity of the nanoparticles. The characteristic peak of kaolinite at 12.398° is completely absent in the synthesized ternary composite due to calcination at high temperatures. The precursors clearly experienced substantial structural reorganization as the ternary composite was formed. The calculation of the average crystallite sizes using the XRD data confirms the nano-size of the nanocomposite by measuring the full width at half maxima (FWHM) in the diffraction patterns, with a size of 83.87 nm. Additional information can be found in the Supplementary Information in Table S2.

3.1.3. SEM and EDS analysis

The FE-SEM micrograph of the synthesized nanocomposite and its particle size distribution is presented in Fig. 3. The average crystallite size or grain size was identified via XRD analysis, we can also have the particle size distribution from the FE-SEM image (Fig. 3(b)). A significant surface area of TiO_2 remains exposed, and the particles appear predominantly spherical shape. Some other

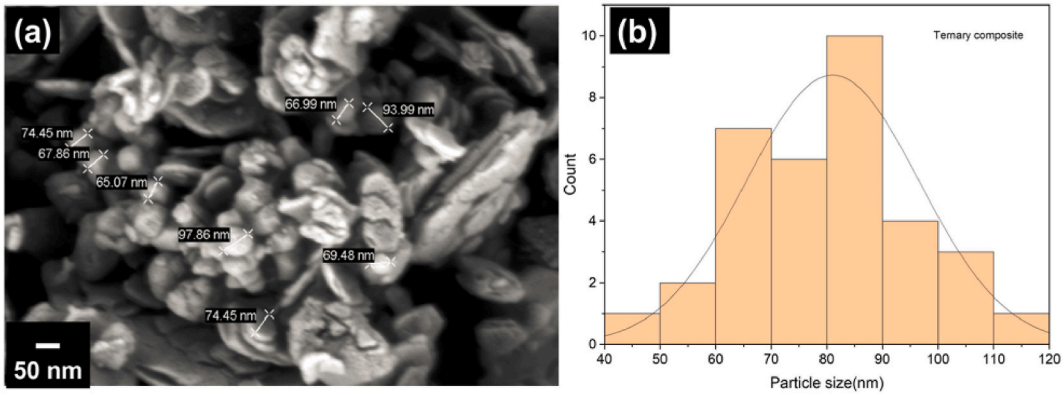

Fig. 3. (a) FE-SEM image of ternary nanocomposite ($K_{65}T_{30}A_5$). (b) Histogram of particle size distribution for the nanocomposite ($K_{65}T_{30}A_5$).

shaped particles are also seen because of a higher portion of kaolinite used in the composite. Despite some degree of agglomeration, FE-SEM is carried out at a magnification of 63000×. To determine the average particle size of the nanoparticles, ImageJ software was employed. For the ternary composite, 35 different locations were marked, and a size distribution histogram (Fig. 3(b) was generated. The average particle size of the photocatalyst is calculated to be approximately 85 nm.

Energy-dispersive X-ray spectroscopy (EDS) was employed to obtain the quantitative information on the element amount, impurities and the distribution of $K_{65}T_{30}A_5$ species in the sample. The EDS spectrum of the nanohybrid is displayed in supplementary information Fig. S2, this observation confirms the presence of four different elements (Al, Si, O, and Ti). Therefore, it can be unequivocally stated that TiO_2, Al_2O_3, and kaolinite were present in the nanocomposite (Fig. S2). EDS analyses were conducted on diverse regions, employing a standard scan spot size area of approximately 3.0 μm^2 across different areas. Consistent results were obtained, revealing an atomic ratio that accurately represented the average composition of Al, Si, and Ti in the $K_{65}T_{30}A_5$ nanocomposites. Notably, the elemental composition derived from the EDS analysis aligned with theoretical calculations. Detailed information, including the elemental composition with mass and atom percentages of the novel nanocomposite, is presented in Table S3 as part of the supporting information.

To confirm the presence of all atoms in the fabricated $K_{65}T_{30}A_5$ nanocomposites, SEM-EDS mapping tests were conducted, providing additional details in the supplementary information (Fig. S3). The distribution of Al, Si, Ti, and O elements in the supplementary information (Fig.S3) further substantiates the existence of all elements, affirming the successful synthesis of ternary nanocomposites. The EDS element mapping profiles in Fig. S3 reveal the Al, Si, Ti, and O elements in ternary nanocomposites, respectively.

3.1.4. *UV–visible diffuse reflectance absorption spectroscopy (DRS) analysis*

Diffuse reflectance spectroscopy (DRS) was used on samples from 190 nm to 900 nm to ascertain the optical behaviour of the nanocomposites. The results are displayed in Fig. 4 with absorption spectra of (a) bare Al_2O_3, (b) pure kaolinite (c) bare TiO_2, and (d) ternary ($K_{65}T_{30}A_5$) nanocomposites. The bandgap was calculated by using Planck's equation, Eg (eV) = 1240/λ (nm), where Eg is the bandgap energy and λ is the corresponding wavelength of the absorption edge. The bandgap value for pure Al_2O_3 and kaolinite is 3.88 eV (320 nm) and 3.27 eV (380 nm) respectively, which are very close to those reported [27,28] agreement. In the case of TiO_2, the bandgap energy value is 3.12 eV (~400 nm) which is very close to the well-known bandgap value of 3.2 eV of pristine TiO_2 [29]. For the ternary ($K_{65}T_{30}A_5$) nanocomposite, the bandgap value of 2.43 eV (510 nm) was found. The composites revealed high reflectance in the visible wavelength with a sharp increase in reflectance at the absorption edge at 400 nm and 510 nm for sample TiO_2 and ternary nanocomposites respectively. The above results suggest that the incorporation of Al_2O_3 is responsible for the visible light photoresponse of the synthesized ternary composite. However, the higher charge carrier recombination is also caused by reduced bandgap energy. Because of this, (kaolinite/TiO_2/Al_2O_3) ternary composite performs better than other kaolinite, Al_2O_3, and TiO_2 in terms of degrading organic dyes.

3.2. *Application of the nanocomposite for dye removal*

3.2.1. *Effect of kaolinite/TiO_2/Al_2O_3 ratio for removal of methylene blue*

The optimum ratio (w/w) of the ternary composite was established based on the evaluation of dye degradation efficiency, and this ratio was verified through batch preparation testing. To determine the optimal concentration of kaolinite, various weight percentages ranging from 30 % to 90 % were utilized, while keeping the same percentages of TiO_2 and Al_2O_3 constant. The findings revealed that a composition comprising 65 % kaolinite, along with 17.5 % each of TiO_2 and Al_2O_3, exhibited better dye degradation properties. Subsequent experiments involved varying the ratio of TiO_2 and Al_2O_3 while maintaining 65 % kaolinite, revealing a consistent increase

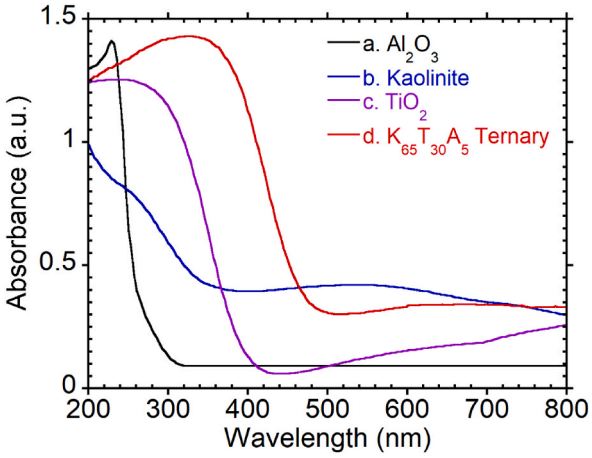

Fig. 4. DRS spectra of (a) Al_2O_3, (b) Kaolinite (c) TiO_2 and synthesized (d) ternary nanocomposite ($K_{65}T_{30}A_5$) samples.

in removal efficiency with higher TiO_2 content (Fig. 5(a)). It is noteworthy that the synergistic effect diminished as the amount of TiO_2 was further increased beyond 30 %. The experimental results (Fig. 5(b)) indicate that a composition consisting of 65 % kaolinite, 30 % TiO_2, and 5 % Al_2O_3, denoted as $K_{65}T_{30}A_5$, exhibited the highest removal efficiency at 97.66 %. The detailed experimental data can be found in Table S4 in the Supplementary Information (SI). Therefore, the ternary composite $K_{65}T_{30}A_5$ is identified as the optimal photocatalyst for this study, demonstrating its potential for efficient dye-pollutant removal.

3.2.2. *Effect of pH for methylene blue and remazol red dye degradation*

The comprehensive analysis of methylene blue degradation efficiency reveals a positive correlation with increasing pH, as illustrated in Fig. 6(a). Within the pH range of 4–12, a notable escalation in removal efficiency is observed, ranging from 56.72 % to 97.66 %. Beyond pH 10, the trend continues to rise steadily. Notably, the optimum pH for methylene blue degradation is identified at pH 9. Detailed experimental data can be found in Table S5 in the Supplementary Information (SI), providing a comprehensive reference for the observed trends and optimum conditions in the degradation process.

To investigate the impact of pH remazol red dye degradation, experiments were conducted by varying the pH from 1 to 9 while keeping other parameters constant. The findings are presented in Fig. 6(b), and detailed experimental data are provided in Table S5 in SI. Overall, degradation efficiency demonstrated an upward trend with increasing pH. Between pH 2.0 and 3.5, a rapid increase in removal efficiency is observed, ranging from 53 % to 90.66 %. Subsequently, the trend exhibits a gradual decline as pH increases. This decline in removal efficiency at higher pH levels (above 7) is attributed to the repulsive force between hydroxyl radicals and anionic RR molecules in alkaline media, along with their competition to reach the nanocomposite surface. It was noted that the maximum percent degradation of dyes occurred at pH 3.5. Since RR is an anionic dye, existing in an aqueous solution with negative charges ($(Dye\text{-}SO_3H) \rightarrow (Dye\text{-}SO_3^-) + H^+$), the positively charged surface of the catalyst at lower pH facilitates easy adsorption of the anionic RR. Consequently, under these conditions, the nanocomposite demonstrates optimal performance in photocatalytic degradation, highlighting the synergistic benefits achieved at pH 3.5.

3.2.3. *Effect of initial dye concertation for methylene blue and remazol red*

As the concentration of methylene blue (MB) increased from 5 ppm to 30 ppm, the degradation efficiency exhibited a gradual decline from 99.09 % to 78.84 %, as illustrated in Fig. 7(a). Detailed experimental data can be found in Table S6 in the Supplementary Information (SI). The reduction in degradation efficiency with elevated dye concentrations is attributed to several factors. Firstly, the increased concentration results in an insufficient supply of active radicals in the sample, hindering the degradation of a significant number of molecules. Additionally, higher molecular densities impede light penetration, preventing photons from reaching the active surface of the catalyst and consequently reducing the efficiency of photo-degradation. Moreover, the elevated concentration of the original MB leads to the generation of additional intermediates, which, in turn, are adsorbed onto the active surface of the catalyst. This process inhibits the production of active radicals and diminishes the number of available active sites in the photocatalyst [30,31].

For RR dye, the investigation into photo-degradation efficiency involved varying the initial dye concentration from 5 ppm to 30 ppm, as depicted in Fig. 7(b). The results show a gradual decrease in degradation efficiency from 80.3 % to 41 % as the concentration of RR dye increases. Simultaneously, the amounts of RR dye removal were determined for each sample, revealing an increase with the rising initial dye concentration. The maximum degradation efficiency, to the initial RR dye concentration, is observed at approximately 10 ppm [32]. A comprehensive set of experimental data is provided in Table S6 in the Supplementary Information (SI), offering detailed insights into the impact of varying initial dye concentrations on the photo-degradation efficiency of RR dye.

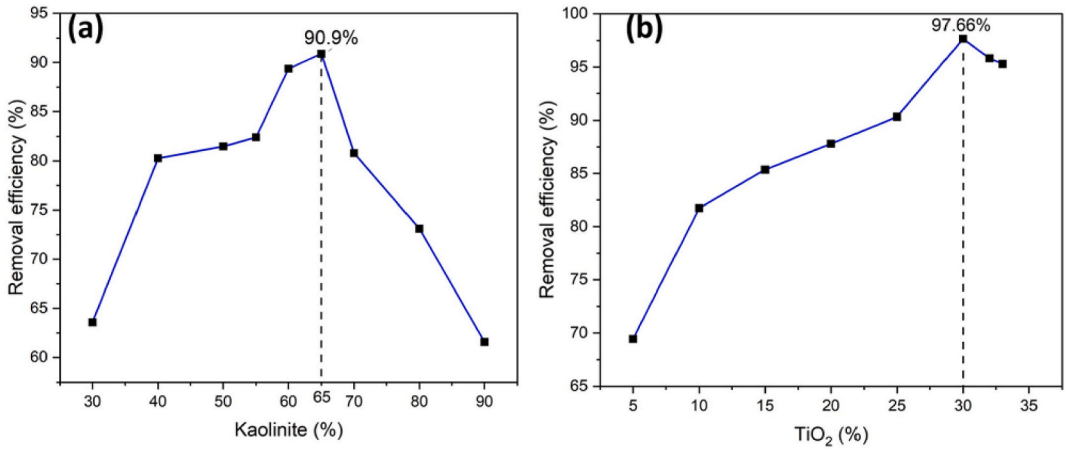

Fig. 5. (a) Effect of kaolinite percentage on the removal of MB taking the same amount of TiO_2 and Al_2O_3 (optimum denoted $K_{65}T_{17.5}A_{17.5}$ composites) (b) Effect of compositional variation of TiO_2 and Al_2O_3 and fixed 65 % kaolinite (optimum denoted $K_{65}T_{30}A_5$) on the photocatalytic degradation of MB.

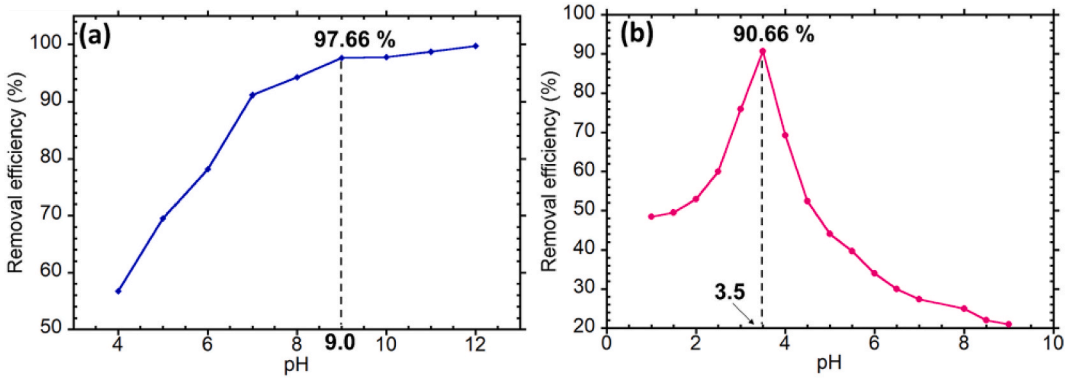

Fig. 6. Effect of pH on removal of (a) Methylene Blue and (b) Remazol Red using the ternary composite ($K_{65}T_{30}A_5$).

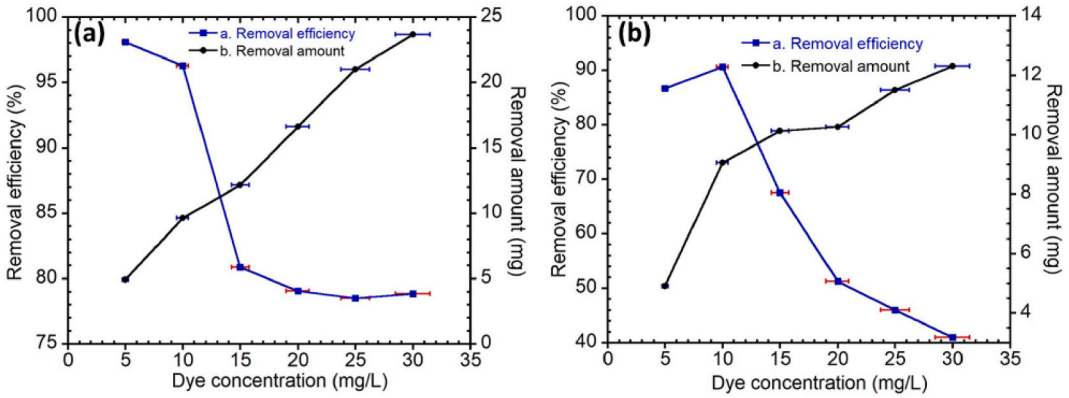

Fig. 7. Effect of initial dye concentration on the removal of (a) Methylene Blue and (b) Remazol Red dye using the ternary composite ($K_{65}T_{30}A_5$).

3.2.4. Effect of irradiation time for methylene blue and remazol red

The removal efficiency of Methylene Blue exhibited a positive correlation with increasing irradiation time. Almost complete removal was achieved within 90 min of irradiation, with a notably faster initial removal rate that gradually slowed over time. Approximately 74.31 % of dye removal occurred within the first 30 min, while 97.67 % was achieved after 90 min of irradiation. The rapid initial removal rate can be attributed to the monolayer adsorption of dye molecules on the nanocomposite surface, possibly coupled with simultaneous photocatalysis. As surface adsorption reaches completion, the removal process transitions to solely photocatalysis, leading to a slight reduction in the removal rate. Another contributing factor could be the decrease in the quantity of dye molecules in the solution as they are progressively removed during the irradiation process [33]. Fig. 8(a) illustrates the efficacy of Methylene Blue (MB) removal using the ternary photocatalyst ($K_{65}T_{30}A_5$) at various irradiation durations (20–100 min) under sunlight exposure. The corresponding experimental data can be found in Table S7 in the Supplementary Information (SI). Notably, the removal

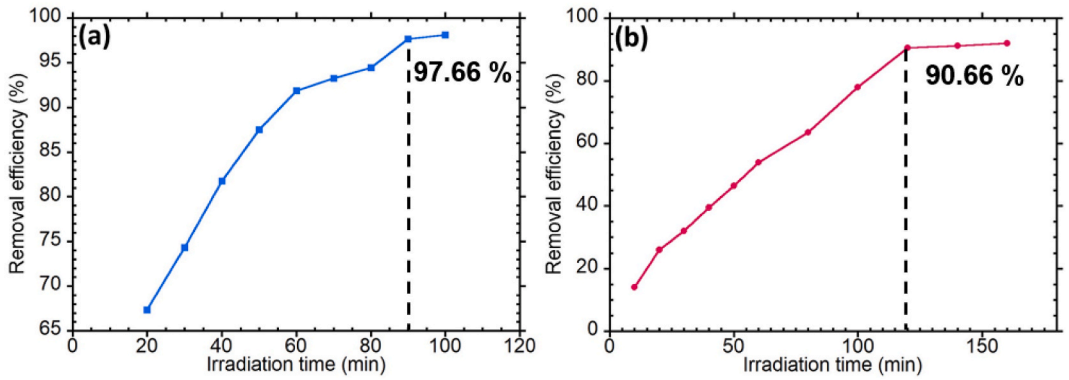

Fig. 8. Effect of irradiation time on the removal of (a) Methylene Blue and (b) Remazol Red dye using the ternary composite.

efficiency reached 97.66 % after 90 min, with a marginal increase to 98.1 % after 100 min. However, this slight increment was deemed insignificant relative to the extended irradiation time. Consequently, 90 min of irradiation time was considered optimal for measuring other effects on the catalytic process, ensuring maximum removal efficiency while minimizing unnecessary prolongation of the experimental duration.

The subsequent Fig. 8(b) illustrates the degradation efficiency of RR dye over varying irradiation durations under optimum conditions and sunlight exposure. The removal efficiency of RR dye increased with prolonged irradiation time, with nearly complete degradation achieved within 120 min. Approximately half of the dye was degraded within 80 min, reaching around 90.6 % removal after 120 min of irradiation. Beyond this point, a slight increase in dye removal efficiency was observed up to 140 min, likely due to the reduction in available dye molecules in the solution.

Near equilibrium, several factors come into play to potentially control the removal process. Firstly, there is increased competition between the remaining dye molecules and intermediate decomposed products to reach the catalyst surface. Secondly, the active sites on the catalyst surface may become deactivated due to the deposition of by-products [34,35].

Detailed data in Table S7 in the Supplementary Information (SI) reveal that the removal efficiency was 90.6 % after 120 min, and it marginally increased to 91.2 % after 140 min. However, this incremental change was considered insignificant in comparison to the extended time. Therefore, 120 min of irradiation time was selected as optimal for investigating additional effects on the catalytic process while ensuring maximum removal efficiency.

3.3. Zeta potential analysis

Based on electrostatic interactions between the dye and the photocatalyst, the influence of pH can be elucidated. The surface charge characteristics of the photocatalyst are determined by the acidity or basicity of the solution, directly impacting its photoactivity. The electrical potential difference between the catalyst's surface and the surrounding medium is referred to as the surface charge, crucial for the photocatalytic reaction and contingent on the presence of hydroxyl groups on the catalyst surface. The point of null surface charge on the photocatalyst is known as the point of zero charge (pH_{PZC}). The catalyst exhibits reduced affinity for dye molecules at the pH_{PZC}. At pH values less than the pH_{PZC}, a protonation reaction occurs, rendering the catalyst surface positively charged; conversely, at pH values greater than the pH_{PZC}, deprotonation takes place, resulting in a negatively charged catalyst surface [36].

Colloidal particles inherently possess an overall surface charge, which significantly influences the adsorption process. Zeta potential (ζ) values of the ternary nanocomposites were measured at different pH levels (ranging from 4 to 12 for MB and 2 to 12 for RR) and are depicted in Fig. 9. The magnitude of ζ serves as an indicator of the surface charge carried by the nanocomposites, with higher or lower values corresponding to increased or decreased electrostatic repulsion between the particles.

According to the literature, pH_{PZC} is about 6.0 for TiO_2 [37], 3.0 for kaolinite [38], and 6.4 for Al_2O_3 [39]. The zero charge point of the synthesized nanocomposite is assumed to lie below pH 7. Also, dyes containing cationic groups, get easily adsorbed when the surface charge of adsorbate is negative (zeta potential of this composite is found to be negative too at pH 9). At pH 9 deprotonation of hydroxyl groups occurred and negative charge dominated at the composite's surface. Consequently, positively charged methylene blue molecules easily got adsorbed due to electrostatic interactions and a higher rate of adsorption made further photocatalysis process simpler and faster [40,41]. This is how better dye removal efficiencies at alkaline media can be explained. The pH at the point of zero charge (pH_{PZC}) for ternary nanocomposites MB degradation was experimentally determined as 9.1.

At pH levels of 2, 2.5, 3.0, 3.5, 4.0, 6, 8, 10, and 12, the zeta potential of the ternary nanocomposite for RR dye is measured. The catalyst exhibits reduced attraction to dye molecules at the point of zero charge (pH_{PZC}). Below pH_{PZC}, a protonation reaction occurs, resulting in a positively charged catalyst surface. Conversely, at pH values above pH_{PZC}, deprotonation occurs, leading to a negatively charged catalyst surface. The experimentally measured zero-charge point for the synthesized nanocomposite is 4.99, as depicted in Fig. 9.

Additionally, since dyes containing anionic groups tend to be easily adsorbed when the surface charge of the adsorbate is positive

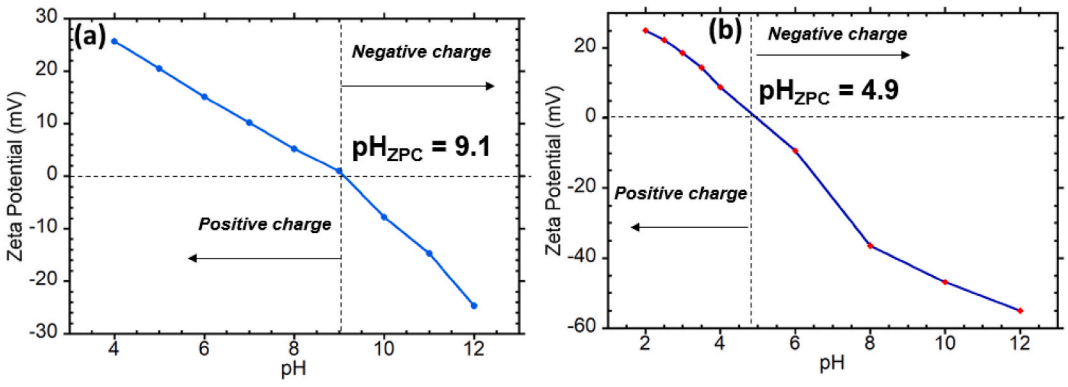

Fig. 9. Zeta potential measurements of ternary nanocomposite in water as a function of different pH values. (a) Methylene blue and (b) Remazol Red.

(the zeta potential of this composite is found to be positive at pH less than 4), at pH 3.5 in Fig. 6(b), protonation of hydroxyl groups occurs, and a positive charge dominates at the composite's surface. Consequently, negatively charged remazol red molecules easily adsorb due to electrostatic interactions, resulting in a higher rate of adsorption and simplifying and accelerating the photocatalysis process. The interactions between the composites and the dye decrease with lowering pH below the zeta potential of the composite, explaining the better dye removal efficiencies observed in acidic media.

3.4. Dye removal mechanism

The mechanism for the photocatalytic degradation of methylene blue and remazol red can be simplified through the use of Fig. 10 and the subsequent steps.

i. The absorption of ultraviolet and/or visible light from the sun caused the promotion of electrons from the valance band to the conduction band leaving behind a positive hole in the valance band. As a result, photoactive electron (e^-_{CB}) and hole ($h^+{}_{VB}$) pairs were generated.

$$\text{Nanocomposite}\ (K_{65}T_{30}A_5) + h\nu \rightarrow h^+_{VB} + e^-_{CB} \quad (3)$$

ii. The photo-generated conduction electron ionized oxygen to produce reactive superoxide ions ($\bullet O^{2-}$) which further produced active species such as hydroxyl ($\bullet$OH) and hydroperoxyl ($\bullet$OOH) radicles via the following reactions [42].

$$e^-_{CB} + O_2 \rightarrow \bullet O^{2-} \quad (4)$$

$$\bullet O_{2-} + 2e^-_{CB} + 2H^+ \rightarrow \bullet OH + OH^- \quad (5)$$

$$\bullet O^{2-} + H_2O \rightarrow \bullet OOH + OH^- \quad (6)$$

iii. The electro-negative species (OH^-) previously generated was neutralized in this step by simply combining them with electro-positive holes. Besides, holes produced protons (H^+) and additional hydroxyl radicles in an aqueous solution.

$$h^+_{VB} + OH^- \rightarrow \bullet OH \quad (7)$$

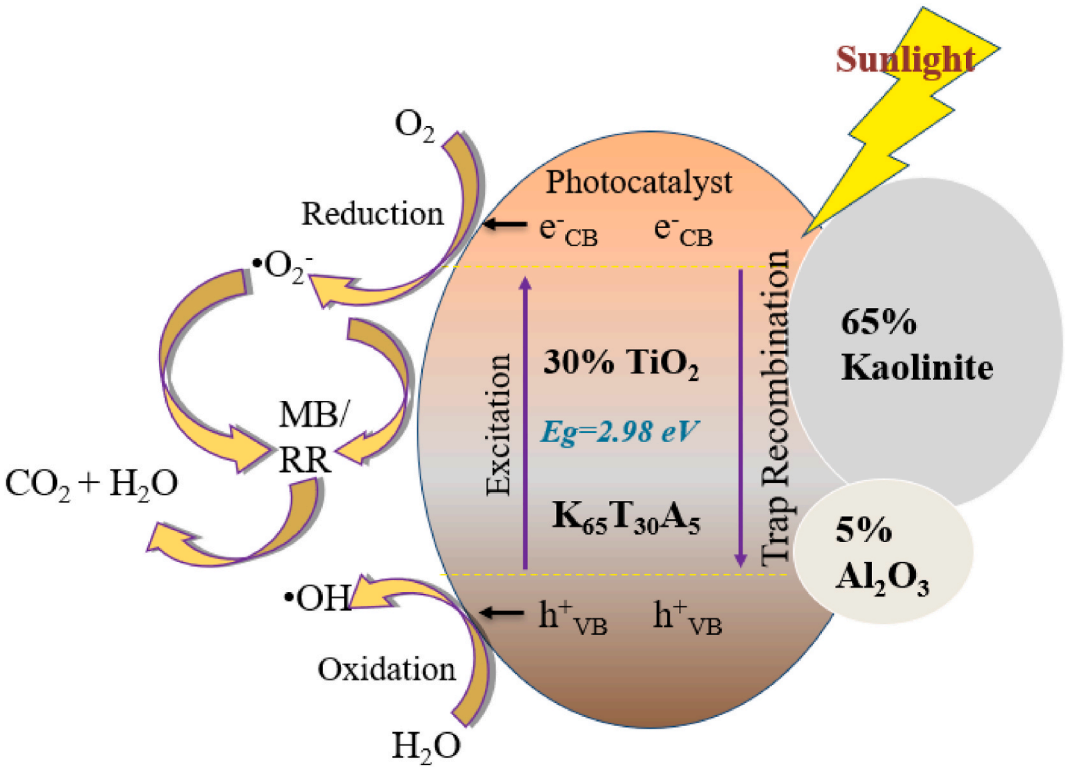

Fig. 10. Mode of action towards photocatalytic degradation of MB and RR with nanocomposite ($K_{65}T_{30}A_5$).

$$h^{+}_{VB} + H_2O \rightarrow \bullet OH + H^{+} \quad (8)$$

iv. Afterwards, hydrogen peroxide (H_2O_2) was formed and zero-valent oxygen was produced as a by-product.

$$2 \bullet OOH \rightarrow H_2O_2 + O_2 \quad (9)$$

v. In this step, hydrogen peroxide immediately decomposed to produce active free radicals causing the reduction of oxygen for the second time.

$$H_2O_2 + e^{-}_{CB} \rightarrow \bullet OH + OH^{-} \quad (10)$$

vi. Finally, the adsorbed molecules of methylene blue were decomposed by the successive oxidative attack of active radicles.

$$\bullet OH + MB \,/\, RR \text{ dye} \rightarrow \text{degradation products} \quad (11)$$

$$\bullet O^{2-} + MB \,/\, RR \text{ dye} \rightarrow \text{degradation products} \quad (12)$$

vii. Direct oxidation of dye molecules could also happen by reacting with holes.

$$h^{+}_{VB} + MB \,/\, RR \text{ dye} \rightarrow \text{degradation products} \quad (13)$$

The overall reaction can be summarized as,

$$h^{+}_{VB} \,/\, \bullet OH \,/\, \bullet O^{2-} + MB \,/\, RR \text{ dye} \rightarrow \text{intermediates} \rightarrow CO_2 + H_2O \quad (14)$$

3.5. Role of radical scavenger

A series of scavenger studies were conducted under optimal conditions to investigate the reactive species involved in the photodegradation of the ternary nanocomposite. Ascorbic acid (AA) ($C_6H_8O_6$), 2-propanol ($(CH_3)_2CHOH$), and di–ammonium oxalate monohydrate (AO) ($(NH_4)_2C_2O_4{\cdot}H_2O$) were used as three separate chemical scavengers to investigate the functions of superoxide radical ion ($\bullet O_2^{-}$), hydroxyl radical (•OH), and photogenerated holes (h^{+}), respectively. The possible contribution of different active species to the degradation of methylene blue/remazol red was being observed by radical trapping experiments. There was decreased photodegradation efficiency at varying levels with the addition of the various scavengers. In the absence of any scavenging agent, the high removal efficiency of 97.66 % was observed by the photocatalyst for MB. On the other hand, on adding di–ammonium oxalate monohydrate (AO) (inhibits h^{+}), 2-propanol (inhibits •OH), and ascorbic acid (AA) (inhibits $\bullet O^{2-}$) separately, dye removal efficiency reduced to 76.56 %, 70.33 %, and 52.27 % respectively. The decrease in the degradation of MB dye is due to the inhibition of active radicals by various scavengers [43]. While all radicals contributed to the degradation of the MB/RR dye, the primary role in the photodegradation of MB was played by ($\bullet O_2^{-}$) radicals rather than (•OH) and h^{+} radicals under sunlight. Consequently, oxidative degradation took place through all plausible pathways described in the previous section.

Fig. 11 (a) illustrates the comparison of removal efficiency of MB and RR dye in each radical trapping experiment and Table S8 in SI contains experimental results. It was revealed that there was decreased photodegradation efficiency at varying levels with the addition of the various scavengers.

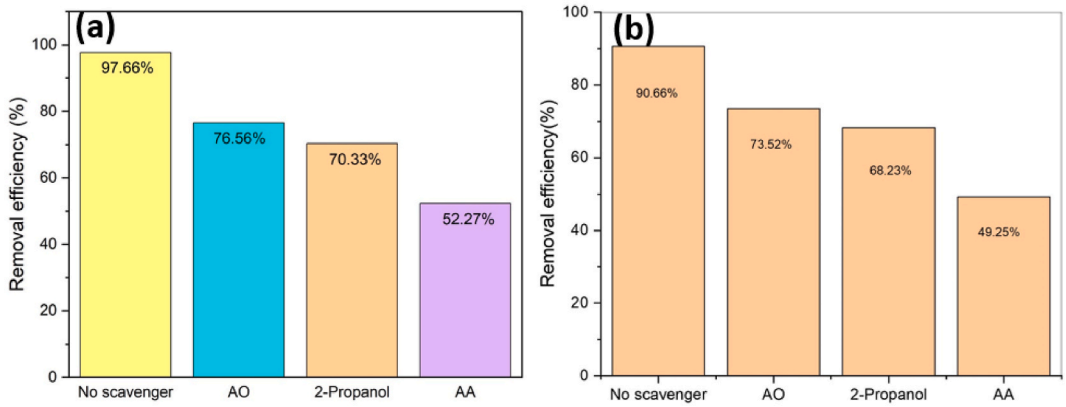

Fig. 11. Comparison of removal efficiency of (a) MB and (b) RR dye in each radical trapping experiment.

In the absence of any scavenging agent, the high removal efficiency of 90.66 % was observed by the photocatalyst for RR shows in Fig. 11 (b). On the other hand, on adding diammonium oxalate monohydrate (AO), 2-propanol, and ascorbic acid (AA) separately, dye removal efficiency reduced to 73.52 %, 68.23 %, and 49.25 % respectively. The decrease in the degradation of RR dye is due to the inhibition of active radicals by various scavengers. Although all the radicals participated in the degradation of the RR dye, the important roles played for the photodegradation of RR were by ($\bullet O_2^-$) radicals rather than the ($\bullet$OH) and h^+ radicals under sunlight. Thus, oxidative degradation occurred in all plausible pathways described in the previous section.

3.6. Photoluminescence detection of hydroxyl radical for photocatalytic dye degradation

The photodegradation mechanism requires the detection of hydroxyl radicals (·OH) formed on the surface of visible light-irradiated ternary nanocomposites using a photoluminescence (PL) technique, with terephthalic acid serving as the probe molecule. Terephthalic acid undergoes a reaction with hydroxyl radicals (·OH) to produce a highly fluorescent product, 2-hydroxyterephthalic acid, during irradiation [44]. The intensity of the PL peak of 2-hydroxyterephthalic acid correlates with the amount of OH radicals generated in water [45,46]. This method relies on the PL signal at 440 nm, indicative of the hydroxylation of terephthalic acid with ·OH generated at the water/$K_{65}T_{30}A_5$ interface.

As depicted in Fig. S4 in supporting information, a gradual increase in fluorescence around 440 nm was observed upon exposure to sunlight in the $K_{65}T_{30}A_5$ solution. This observation strongly indicates that the fluorescence arises from chemical reactions involving terephthalic acid and ·OH radicals formed at the $K_{65}T_{30}A_5$/water interface through photocatalytic reactions.

3.7. Rate kinetics investigation of the removal of methylene blue with synthesized nanocomposite ($K_{65}T_{30}A_5$)

The simplified form of the Langmuir-Hinshelwood model to the apparent pseudo-first-order kinetics is shown in Eq. (1).

$$\ln(C_o / C_t) = k_{app}\, t \tag{15}$$

where C_o is the initial concentration of ppm (10 ppm), C_t is the concentration of MB and RR at various contact times (ppm), k_{app} is the apparent rate constant (min^{-1}). The value apparent rate constant (k_{app}) was calculated from the plot of ln (C_o/C_t) vs. time (Fig. 12).

The values of $k_{app} = 0.03607$ and $R^2 = 0.97939$ for MB and $k_{app} = 1.5523$ and $R^2 = 0.68163$ were found respectively. The higher correlation coefficient indicates that the proposed kinetic model was in good agreement with our experimental data i.e. the photocatalytic degradation of both Methylene Blue and Remazol Red by the nanocomposite followed pseudo-first-order kinetics. The significant value of k_{app} indicates a rapid removal of Methylene Blue and RR dye respectively.

3.8. Reusability/recyclability analysis

The results of the reusability experiments demonstrated nearly identical efficiency under optimum conditions for up to four cycles. These findings are illustrated in the bar chart presented in Fig. 13. The nanocomposite demonstrated excellent removal efficiency for up to three cycles, after which a gradual decline was observed. This decrease in effectiveness is likely due to degradation byproducts hindering the catalyst's active sites, thereby impeding solar radiation absorption on its surface. Furthermore, material loss during repeated washing cycles may also play a role in this performance decline [47,48].

However, the nanocomposite material exhibited promising potential for repeated and long-term application in dye removal from wastewater. Its utilization of inexpensive kaolinite in significant quantities, combined with its capability for nearly complete and rapid removal of acid and basic azo dye alongside long-term reusability, strongly indicates its suitability for industrial-scale applications. The performance of reusability can be improved by washing the used nanocomposite with acid to remove the more adsorbed dye. However,

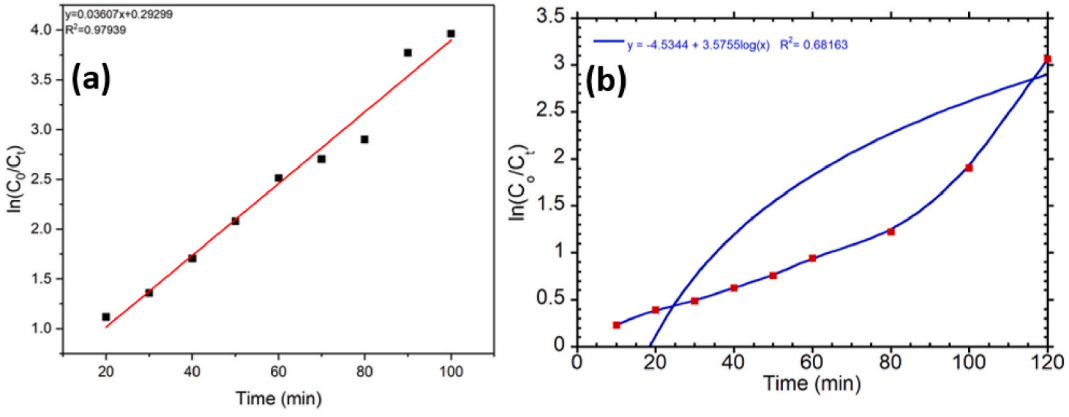

Fig. 12. Ln (C_o/C_t) vs. time plot to find out the kinetic parameters of (a) MB and (b) RR.

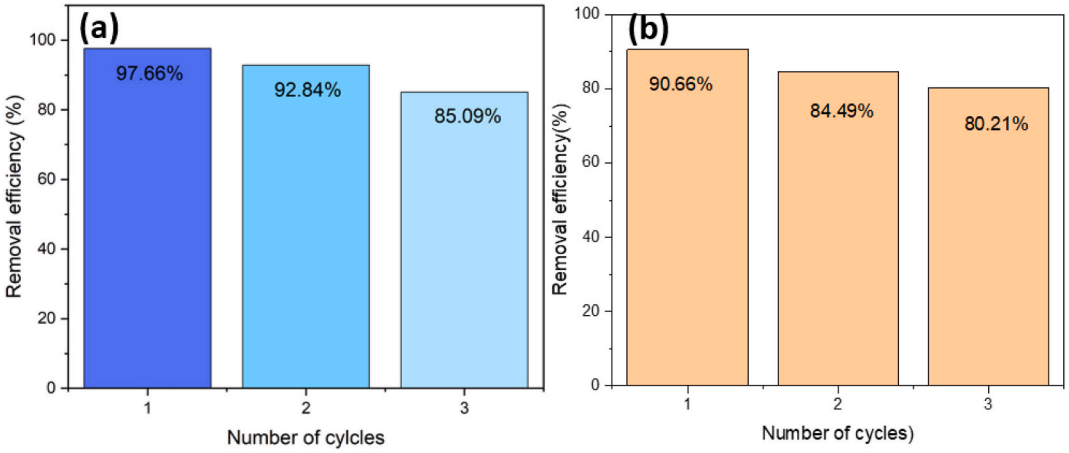

Fig. 13. Demonstration of reusability of the nanocomposite for the removal of (a) Methylene Blue and (b) Remazol Red up to three cycles.

it will make the process more costly.

For industrial applications, a material's ability to withstand repeated long-term use while maintaining efficiency is crucial, as it improves cost-effectiveness and feasibility of the process. In this research, we evaluated a newly developed nanohybrid material over four cycles and found it consistently efficient under optimal conditions. Regeneration was straightforward, involving thorough washing with distilled water followed by drying after each cycle.

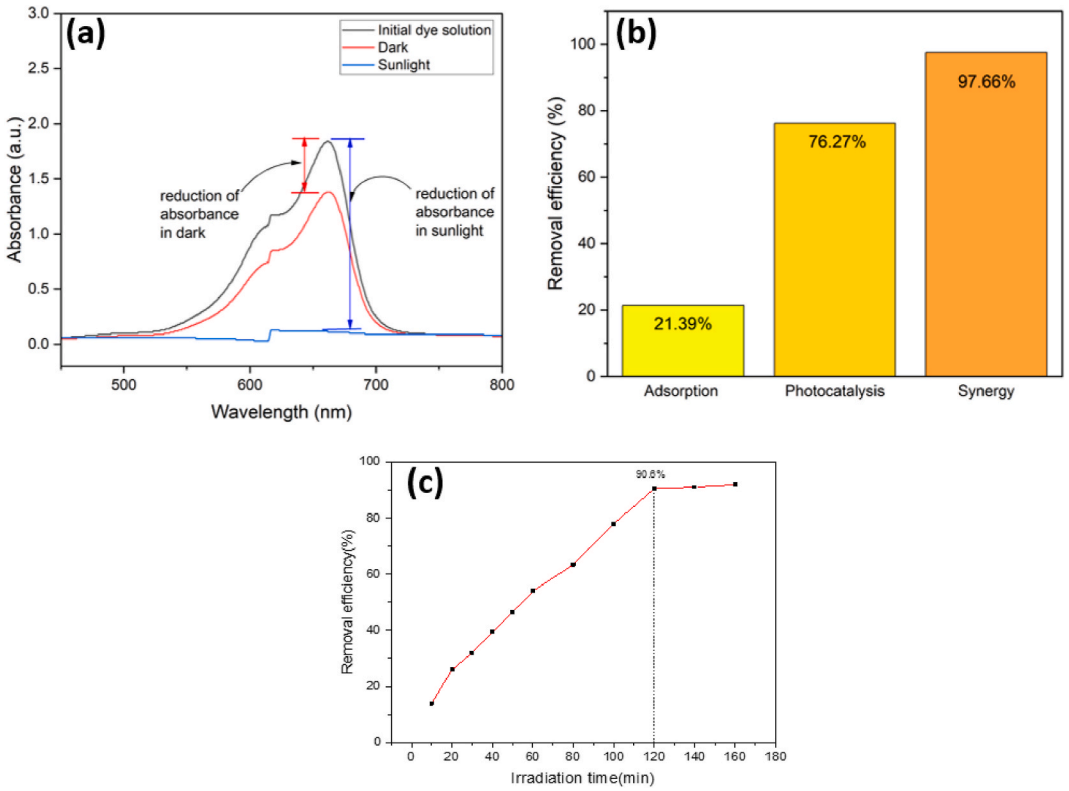

Fig. 14. Comparison of the removal efficiency of MB by synthesized ternary composite ($K_{65}T_{30}A_5$) in sunlight and dark. (a) Absorbance spectra showing dye solutions before and after conducting control experiments of MB, (b) MB removal efficiency considering either adsorption or photocatalysis, along with their synergistic effect and (c) effect of irradiation time on removal of RR dye using the ternary composite.

3.9. Control experiment analysis

The contribution of adsorption and photocatalysis processes towards dye removal was investigated by conducting distinct experiments either in the dark or under sunlight irradiation for one and a half hours under optimized operating conditions. The results of the control experiments are illustrated in Fig. 14.

It is clear from Fig. 14(b) that 97.66 % and 21.39 % dye removal efficiencies were obtained with and without sunlight respectively. So, the subtraction of either value, i.e. 76.27 % dye removal was due to photocatalysis and 21.39 % dye removal occurred by adsorption. In Fig. 14(a), the red bar indicates dye removal efficiency by adsorption whereas the blue bar indicates the synergistic effect of adsorption and photocatalysis. The synthesized ternary composite ($K_{65}T_{30}A_5$) proved to be an excellent photocatalyst for degrading methylene blue, yet adsorptive properties were not significant. Only adsorption at the surface was possible due to electrostatic interactions between oppositely charged compounds in alkaline aqueous solution. This can be a plausible explanation of the outcome of control experiments. Additional experiments regarding photolysis of MB dye under direct sunlight without any catalyst were conducted. Nearly 26.27 % photolysis of MB dye without any catalyst was obtained. So, under the experimental conditions sunlight itself has a significant contribution to the degradation process.

Fig. 14(c) illustrates the degradation efficiency of RR dye over time under optimal conditions during sunlight irradiation. The removal efficiency of RR dye increased proportionally with the extension of irradiation time. Nearly complete degradation was achieved within 120 min. Specifically, more than half of the dye was degraded within the first 80 min, and approximately 90.6 % of the dye was removed by the 120th minute of irradiation. Beyond this duration, spanning up to 140 min, a marginal improvement in dye removal efficiency was noted due to the diminishing concentration of dye molecules present in the solution.

Approaching equilibrium, various factors come into play in controlling the removal process. Firstly, there is heightened competition between the remaining dye molecules in the solution and intermediate degraded products to reach the catalyst surface. Secondly, the active sites on the catalyst surface become deactivated due to the deposition of by-products [49].

It is noteworthy that the removal efficiency was 90.6 % after 120 min, and only a marginal increase to 91.2 % was observed after 140 min. This minor increment, deemed insignificant relative to the elapsed time, led to the conclusion that 120 min of irradiation time was considered optimal for measuring other effects on the catalytic process with maximum removal efficiency.

3.10. Total organic carbon (TOC) analysis

Total organic carbon analysis (TOC) provides an estimation of the amount of carbon bound to organic compounds. This may be used to determine the degree to which the dye molecules are broken down during photocatalysis. The result of the TOC analysis for MB was found 8.12 mg/L in initial dye solution and 3.89 mg/L in the final solution with the reduction efficiency of 52.09 %. The result of the TOC analysis for RR was found 8.32 mg/L in initial solution and 3.87 mg/L in the final solution with the reduction efficiency of 53.48 %. It is evident from the TOC removal values that less than 50 % of organic degradation by-products remained in the solution after 90 min of irradiation. The higher removal efficiency (that is 97.66 % for MB) compared to the TOC removal value (52.09 % for MB) suggests that the dye molecules were broken down into smaller colorless products first before being mineralized to carbon dioxide, water and other inorganic species. Similar trend was observed in case of RR degradation. These residual organic materials might require extended irradiation times to ensure their complete mineralization [50,51].

The estimation of carbon associated with organic substances can be conducted through total organic carbon analysis (TOC). In the context of evaluating the mineralization of RR dye, TOC was measured to assess the extent of RR molecule degradation during photocatalysis. Higher TOC removal values signify the complete mineralization of organic dye contaminants, a desirable outcome in photocatalysis to mitigate the generation of potentially harmful byproducts [35].

The TOC removal values indicate that after 120 min of irradiation, less than 50 % of organic degradation by-products remained in the solution. Notably, the higher removal efficiency (90.66 %) in comparison to the TOC removal value (53.48 %) suggests that the dye molecules underwent initial breakdown into smaller, colorless products before being fully mineralized to carbon dioxide, water, and other inorganic species. The presence of residual organic materials implies that extended irradiation times may be necessary to ensure their complete mineralization [35,36].

Table 1 presents a comprehensive comparison of the photocatalytic activity of recently reported nanocomposites containing kaolinite, TiO_2, and/or Al_2O_3, along with the synthesized nanocomposite ($K_{65}T_{30}A_5$), for the removal of MB and RR. The performance of the novel nanocomposite is assessed in terms of removal efficiency, catalyst loading, irradiation time, and the light source utilized.

4. Conclusion

This research provides valuable insights into the effectiveness of a novel nanocomposite in the removal of harmful dyes such as Methylene Blue and Remazol Red from industrial wastewater. This study presents a straightforward and economical approach for fabricating ternary nanocomposites at ambient temperature (25 °C), employing a relatively simple and affordable procedure. The ternary composite $K_{65}T_{30}A_5$ that was prepared with 65 % kaolinite, 30 % TiO_2 and 5 % Al_2O_3 showed maximum removal efficiency for the Methylene Blue (cationic) and Remazol Red (anionic). The maximum dye removal efficiency of 97.67 % was achieved at the initial Methylene Blue concentration of 10 ppm, pH 9 for fixed catalyst dosing (0.2 g/L) and contact time of 90 min whereas the highest dye removal efficiency of 90.66 % for Remazol Red was attained at a concentration of 10 ppm, pH 3.5, fixed catalyst dosing (0.4 g/L), and contact period of 120 min. The scavenger test showed that the probable active free radicals for the MB degradation were $\bullet O^{2-}$ and •OH. The kinetic study showed that the degradation of MB and RR follows pseudo-first order rate of kinetics and Langmuir-

Table 1
Comparison of photocatalytic activity of recently reported nanocomposites containing kaolinite, TiO_2 and/or Al_2O_3 and synthesized nanocomposite ($K_{65}T_{30}A_{05}$) for MB and RR removal.

Photocatalyst	Dye conc.	Photocatalyst loading	Time min	Light source	Removal efficiency %	Ref.
Kaolinite-TiO_2-Al_2O_3	10 mg/L	0.2 g/L	90	Solar light	97.66	Present study (MB)
Kaolinite-TiO_2-Al_2O_3	10 mg/L	0.4 g/L	120	Solar light	90.66	Present study (RR)
Kaolinite/TiO_2 Nanohybrid	20 mg/L	1.5 g/L	180	UV-C	97	[52]
TiO_2/Kaolinite composite	100 mg/L	–	300	UV light	95	[53]
Natural clay/titania composite	50 mg/L	2.5 g/L	180	UV-A lamp (9 W)	84.1	[54]
Commercial kaolinite (KGa-1b)	20 mmol/L	0.2 g/L	40	UV-A (8 W)	65	[55]
ZnO/TiO_2 Heterojunction nanomesh	12 mg/L		120	Xenon lamp (500 W)	92	[56]
ZnO–TiO_2 composites	20 mmol/L	30 mg/60 mL	360	UV lamp	82	[57]
CuO/Al_2O_3 composite	100 mg/L	0.1 mg/L	100	UV lamp	90	[58]
Pd–ZnO/Kaolinite composite	5 mg/L	0.4 g/L	60	UV light Hg lamp-530 W	98	[59]
Kaolinite/TiO_2 composite	25 mg/L	10 g/L	5	UV light, 365 nm, 30 W	99	[60]

M. Abdulla- Al-Mamun et al.

Hinshelwood model. The scavenger test was used to establish a possible photocatalytic degradation mechanism for the MB and RR using the composite, and it was found that the probable active free radicals for the RR degradation were $\bullet O_2^-$. The very fast, economic and nearly complete removal process of Methylene Blue and Remazol Red from the aqueous solution by reusable ternary composite was the fascinating feature of this study as compared to photocatalytic degradation processes as referred to in the compiled Table 1. Therefore, this study has demonstrated significant promise for the extensive application of this new nanocomposite in the removal of hazardous dye pollutants from industrial waste water. Finally, this study has demonstrated great promise for the general use of this innovative nanocomposite in eliminating harmful dye pollutants from industrial effluents. This study establishes a strong foundation for future research and application development in the field of nanocomposite photocatalysis for environmental dye remediation.

Funding

This work was supported by the Ministry of Science and Technology grant under order no. 39.00.0000.009.14.019.21-EAS-487 for Project ID: SRG-222389, provided by the Government of the People's Republic of Bangladesh.

Availability of data and materials

This manuscript contains all of the data generated or analyzed during this research.

CRediT authorship contribution statement

Nadira Parvin Lata: Writing – original draft, Investigation, Formal analysis, Data curation. **Md Sheum Hussain:** Writing – original draft, Investigation, Formal analysis, Data curation. **Md Abdulla-Al-Mamun:** Writing – review & editing, Writing – original draft, Supervision, Project administration, Methodology, Investigation, Funding acquisition, Conceptualization. **Taslim Ur Rashid:** Visualization, Validation, Supervision, Investigation. **Sayed Md Shamsuddin:** Writing – review & editing, Supervision, Project administration, Funding acquisition, Conceptualization.

Declaration of competing interest

The authors declare that they have no known competing financial interests or personal relationships that could have appeared to influence the work reported in this paper.

Acknowledgements

The authors extend their sincere appreciation to the Ministry of Science and Technology, Government of the People's Republic of Bangladesh, for the invaluable financial support that significantly contributed to the successful completion of this research project. Additionally, we would like to express our gratitude for the required analytical and technical support offered by the Centre for Advanced Research in Sciences (CARS), Dhaka University and the Bangladesh Council for Scientific and Industrial Research (BCSIR).

Appendix A. Supplementary data

Supplementary data to this article can be found online at https://doi.org/10.1016/j.heliyon.2024.e29255.

References

[1] A. Ahmad, S.H. Mohd-Setapar, C.S. Chuong, A. Khatoon, W.A. Wani, R. Kumar, M. Rafatullah, Recent advances in new generation dye removal technologies: novel search for approaches to reprocess wastewater, RSC Adv. 5 (39) (2015) 30801–30818, https://doi.org/10.1039/C4RA16959J.

[2] S.C. Dey, M. Al-Amin, T.U. Rashid, M. Ashaduzzaman, S.M. Shamsuddin, pH induced fabrication of kaolinite-chitosan biocomposite, Int. Lett. Chem. Phys. Astron. 68 (2016) 1–9, https://doi.org/10.18052/www.scipress.com/ILCPA.68.1.

[3] M. Ikeda, Y. Kusumoto, H. Yang, S. Somekawa, H. Uenjyo, M. Abdulla-Al-Mamun, Y. Horie, Photocatalytic hydrogen production enhanced by laser ablation in water-methanol mixture containing titanium (IV) oxide and graphite silica, Catal. Commun. 9 (6) (2008) 1329–1333, https://doi.org/10.1016/j.catcom.2007.11.026.

[4] E.O. Ichipi, A.B. Mapossa, A.C.F. Costa, E.M. Chirwa, S.M. Tichapondwa, Fabrication and characterization of recyclable, magnetic (CoFe2O4) x/Ag2S-ZnO composites for visible-light-induced photocatalytic degradation of methylene blue dye, J. Water Process Eng. 54 (2023) 104040, https://doi.org/10.1016/j.jwpe.2023.104040.

[5] M. Abdulla-Al-Mamun, Y. Kusumoto, T. Zannat, M.S. Islam, Synergistic enhanced photocatalytic and photothermal activity of Au@ TiO_2 nanopellets against human epithelial carcinoma cells, Phys. Chem. Chem. Phys. 13 (47) (2011) 21026–21034, https://doi.org/10.1039/C1CP22683E.

[6] A.L. Linsebigler, G. Lu, J.T. Yates Jr., Photocatalysis on TiO_2 surfaces: principles, mechanisms, and selected results, Chem. Rev. 95 (3) (1995) 735–758, https://doi.org/10.1021/cr00035a013.

[7] M.R. Hoffmann, S.T. Martin, W. Choi, D.W. Bahnemann, Environmental applications of semiconductor photocatalysis, Chem. Rev. 95 (1) (1995) 69–96, https://doi.org/10.1021/cr00033a004.

[8] M. Anpo, M. Takeuchi, The design and development of highly reactive titanium oxide photocatalysts operating under visible light irradiation, J. Catal. 216 (1–2) (2003) 505–516, https://doi.org/10.1016/S0021-9517(02)00104-5.

[9] M. Faramarzpour, M. Vossoughi, M. Borghei, Photocatalytic degradation of furfural by titania nanoparticles in a floating-bed photoreactor, Chem. Eng. J. 146 (1) (2009) 79–85, https://doi.org/10.1016/j.cej.2008.05.033.

[10] V. Vimonses, M.N. Chong, B. Jin, Evaluation of the physical properties and photodegradation ability of titania nanocrystalline impregnated onto modified kaolin, Microporous Mesoporous Mater. 132 (1–2) (2010) 201–209, https://doi.org/10.1016/j.micromeso.2010.02.021.

[11] A.K.M.M. Hasan, et al., A kaolinite/TiO_2/ZnO-based novel ternary composite for photocatalytic degradation of anionic azo dyes, Bull. Mater. Sci. 43 (1) (2020) 1–9, https://doi.org/10.1007/s12034-019-1964-4.

[12] A.T. Famojuro, I.A.O. Ojo, G.O. Egharevba, M.A. Maaza, Sol-gel/hydrothermal synthesis of mixed metal oxide of titanium and zinc nanocomposites through direct chemical method, IFE J. Sci. 15 (2) (2013) 321–329.

[13] K.M. Kutláková, et al., Preparation and characterization of photoactive composite kaolinite/TiO_2, J. Hazard. Mater. 188 (1–3) (2011) 212–220, https://doi.org/10.1016/j.jhazmat.2011.01.106.

[14] J. da Silva Lopes, et al., Modification of kaolinite from Pará/Brazil region applied in the anionic dye photocatalytic discoloration, Appl. Clay Sci. 168 (2019) 295–303, https://doi.org/10.1016/j.clay.2018.11.028.

[15] D. Gupta, R. Chauhan, N. Kumar, V. Singh, V.C. Srivastava, P. Mohanty, T.K. Mandal, Enhancing photocatalytic degradation of quinoline by ZnO: TiO_2 mixed oxide: optimization of operating parameters and mechanistic study, J. Environ. Manag. 258 (2020) 110032, https://doi.org/10.1016/j.jenvman.2019.110032.

[16] L. Munguti, F. Dejene, Influence of annealing temperature on structural, optical and photocatalytic properties of ZnO–TiO_2 composites for application in dye removal in water, Nano-Struct. Nano-Obj. 24 (2020) 100594, https://doi.org/10.1016/j.nanoso.2020.100594.

[17] P. Zamostny, Z. Belohlav, Identification of kinetic models of heterogeneously catalyzed reactions, Appl. Catal. Gen. 225 (1–2) (2002) 291–299, https://doi.org/10.1016/S0926-860X(01)00875-4.

[18] T.H.D. Silva, A.O. Ribeiro, E.J. Nassar, R. Trujillano, V. Rives, M.A. Vicente, E.H.D. Faria, K.J. Ciuffi, Kaolinite/TiO_2/cobalt (II) tetra carboxy metallophthalocyanine nanocomposites as heterogeneous photocatalysts for decomposition of organic pollutants trimethoprim, caffeine and prometryn, J. Braz. Chem. Soc. 30 (2019) 2610–2623, https://doi.org/10.21577/0103-5053.20190178.

[19] C.H. Bai, S.L. Zheng, Z.M. Sun, S.M. Lei, J.Y. Gui, F.L. Lv, M. Wen, TiO_2/Kaolinite photocatalytic material of Fe^{3+} chemical doping and Fe_2O_3 heat-banding and its mechanism analysis, Adv. Mater. Res. 178 (2011) 324–329, https://doi.org/10.4028/www.scientific.net/AMR.178.324.

[20] C. Wang, H. Shi, P. Zhang, Y. Li, Synthesis and characterization of kaolinite/TiO_2 nano-photocatalysts, Appl. Clay Sci. 53 (4) (2011) 646–649, https://doi.org/10.1016/j.clay.2011.05.017.

[21] A.R. Chowdhuri, C.G. Takoudis, Investigation of the aluminum oxide/Si (100) interface formed by chemical vapor deposition, Thin Solid Films 446 (1) (2004) 155–159, https://doi.org/10.1016/S0040-6090(03)01311-7.

[22] P. Padmaja, G.M. Anilkumar, P. Mukindan, G. Aruldhas, K.G.K. Warrier, Characterisation of stoichiometric sol-gel mullite by fourier transform infrared spectroscopy, Int. J. Inorg. Mater. 3 (7) (2001) 693–698, https://doi.org/10.1016/S1466-6049(01)00189-1.

[23] H. Zhu, et al., Effective photocatalytic decolorization of methyl orange utilizing TiO_2/ZnO/chitosan nanocomposite films under simulated solar irradiation, Desalination 286 (2012) 41–48, https://doi.org/10.1016/j.desal.2011.10.036.

[24] B. Ekka, M.K. Sahu, R.K. Patel, P. Dash, Titania coated silica nanocomposite prepared via encapsulation method for the degradation of safranin-O dye from aqueous solution: optimization using statistical design, Water Resour. Ind. 22 (2019) 100071, https://doi.org/10.1016/j.wri.2016.08.001.

[25] W.J. Wolfgong, Chemical analysis techniques for failure analysis: Part 1, common instrumental methods, in: Handbook of Materials Failure Analysis with Case Studies from the Aerospace and Automotive Industries, Elsevier, 2016, pp. 279–307, https://doi.org/10.1016/B978-0-12-800950-5.00014-4.

[26] R. Saravanan, J. Aviles, F. Gracia, E. Mosquera, V.K. Gupta, Crystallinity and lowering band gap induced visible light photocatalytic activity of TiO_2/CS (Chitosan) nanocomposites, Int. J. Biol. Macromol. 109 (2018) 1239–1245, https://doi.org/10.1016/j.ijbiomac.2017.11.125.

[27] Y. Hu, Y. Wang, X. Yu, Enhancement of nonlinear optical properties of composite material based on Al_2O_3 by iron, Europhys. Lett. 108 (5) (2014) 54005, https://doi.org/10.1209/0295-5075/108/54005.

[28] C. Wang, H. Shi, P. Zhang, Y. Li, Synthesis and characterization of kaolinite/TiO2 nano-photocatalysts, Appl. Clay Sci. 53 (4) (2011) 646–649, https://doi.org/10.1016/j.clay.2011.05.017.

[29] M. Abdulla-Al-Mamun, Y. Kusumoto, M.S. Islam, Enhanced photocatalytic cytotoxic activity of Ag@ Fe-doped TiO2 nanocomposites against human epithelial carcinoma cells, J. Mater. Chem. 22 (12) (2012) 5460–5469, https://doi.org/10.1039/C2JM15636A.

[30] M.R.D. Khaki, M.S. Shafeeyan, A.A.A. Raman, W.M.A.W. Daud, Evaluating the efficiency of nano-sized Cu doped TiO_2/ZnO photocatalyst under visible light irradiation, J. Mol. Liq. 258 (2018) 354–365, https://doi.org/10.1016/j.molliq.2017.11.030.

[31] Z. Gao, T.J. Bandosz, Z. Zhao, M. Han, J. Qiu, Investigation of factors affecting adsorption of transition metals on oxidized carbon nanotubes, J. Hazard. Mater. 167 (1–3) (2009) 357–365, https://doi.org/10.1016/j.jhazmat.2009.01.050.

[32] F. Azeez, E. Al-Hetlani, M. Arafa, Y. Abdelmonem, A.A. Nazeer, M.O. Amin, M. Madkour, The effect of surface charge on photocatalytic degradation of methylene blue dye using chargeable titania nanoparticles, Sci. Rep. 8 (1) (2018) 7104, https://doi.org/10.1038/s41598-018-25673-5.

[33] P. Bindu, S. Thomas, Estimation of lattice strain in ZnO nanoparticles: X-ray peak profile analysis, J. Theor. Appl. Phys. 8 (4) (2014) 123–134, https://doi.org/10.1007/s40094-014-0141-9.

[34] K. Bellir, M. Bencheikh-Lehocine, A.H. Meniai, Removal of methylene blue from aqueous solutions using an acid activated Algerian bentonite: equilibrium and kinetic studies, Int. Renew. Energy Congr. 2010 (2010) 360–367.

[35] I.K. Konstantinou, T.A. Albanis, TiO_2-assisted photocatalytic degradation of azo dyes in aqueous solution: kinetic and mechanistic investigations: a review, Appl. Catal. B Environ. 49 (1) (2014) 1–14, https://doi.org/10.1016/j.apcatb.2003.11.010.

[36] M.R.D. Khaki, M.S. Shafeeyan, A.A.A. Raman, W.M.A.W. Daud, Evaluating the efficiency of nano-sized Cu doped TiO_2/ZnO photocatalyst under visible light irradiation, J. Mol. Liq. 258 (2018) 354–365, https://doi.org/10.1016/j.molliq.2017.11.030.

[37] M. Zhu, H. Wang, A.A. Keller, T. Wang, F. Li, The effect of humic acid on the aggregation of titanium dioxide nanoparticles under different pH and ionic strengths, Sci. Total Environ. 487 (2014) 375–380, https://doi.org/10.1016/j.scitotenv.2014.04.036.

[38] M. Tschapek, L. Tcheichvili, C. Wasowski, The point of zero charge (pzc) of kaolinite and SiO_2+ AI_2O_3 mixtures, Clay Miner. 10 (4) (1974) 219–229, https://doi.org/10.1180/claymin.1974.010.4.01.
[39] P. V Brady, Alumina surface chemistry at 25, 40, and 60 C, Geochem. Cosmochim. Acta 58 (3) (1994) 1213–1217, https://doi.org/10.1016/0016-7037(94)90586-X.
[40] F. Azeez, E. Al-Hetlani, M. Arafa, Y. Abdelmonem, A.A. Nazeer, M.O. Amin, M. Madkour, The effect of surface charge on photocatalytic degradation of methylene blue dye using chargeable titania nanoparticles, Sci. Rep. 8 (1) (2018) 1–9, https://doi.org/10.1038/s41598-018-25673-5.
[41] R.A. Rather, S. Singh, B. Pal, Photocatalytic degradation of methylene blue by plasmonic metal-TiO_2 nanocatalysts under visible light irradiation, J. Nanosci. Nanotechnol. 17 (2) (2017) 1210–1216, https://doi.org/10.1166/jnn.2017.12658.
[42] D. Gupta, et al., Enhancing photocatalytic degradation of quinoline by ZnO: TiO2 mixed oxide: optimization of operating parameters and mechanistic study, J. Environ. Manag. 258 (2020) 110032, https://doi.org/10.1016/j.jenvman.2019.110032.
[43] R. Jiang, H. Zhu, X. Li, L. Xiao, Visible light photocatalytic decolourization of CI Acid Red 66 by chitosan capped CdS composite nanoparticles, Chem. Eng. J. 152 (2–3) (2009) 537–542, https://doi.org/10.1016/j.cej.2009.05.037.
[44] M. Abdulla-Al-Mamun, Y. Kusumoto, M.S. Islam, Enhanced photocatalytic cytotoxic activity of Ag@ Fe-doped TiO_2 nanocomposites against human epithelial carcinoma cells, J. Mater. Chem. 22 (12) (2012) 5460–5469, https://doi.org/10.1039/C2JM15636A.
[45] J. Yu, W. Wang, B. Cheng, B. Su, Enhancement of photocatalytic activity of mesporous TiO_2 powders by hydrothermal surface fluorination treatment, J. Phys. Chem. C 113 (2009) 6743–6750, https://doi.org/10.1021/jp900136q.
[46] K. Ishibashi, A. Fujishima, T. Watanabe, K. Hashimoto, Detection of active oxidative species in TiO2 photocatalysis using the fluorescence technique, Electrochem. Commun. 2 (2000) 207–210, https://doi.org/10.1016/S1388-2481(00)00006-0.
[47] R. Jiang, H. Zhu, G. Zeng, L. Xiao, Y. Guan, Synergy of adsorption and visible light photocatalysis to decolor methyl orange by activated carbon/nanosized CdS/chitosan composite, J. Cent. South Univ. Technol. 17 (6) (2010) 1223–1229, https://doi.org/10.1007/s11771-010-0623-0.
[48] I.K. Konstantinou, T.A. Albanis, TiO_2-assisted photocatalytic degradation of azo dyes in aqueous solution: kinetic and mechanistic investigations: a review, Appl. Catal. B Environ. 49 (1) (2004) 1–14, https://doi.org/10.1016/j.apcatb.2003.11.010.
[49] K. Bellir, M. Bencheikh-Lehocine, A.H. Meniai, Removal of methylene blue from aqueous solutions using an acid activated Algerian bentonite: equilibrium and kinetic studies, Int. Renew. Energy Congr. 2010 (2010) 360–367.
[50] G. Mamba, M.A. Mamo, X.Y. Mbianda, A.K. Mishra, Nd, N, S-TiO_2 decorated on reduced graphene oxide for a visible light active photocatalyst for dye degradation: comparison to its MWCNT/Nd, N, S-TiO_2 analogue, Ind. Eng. Chem. Res. 53 (37) (2014) 14329–14338, https://doi.org/10.1021/ie502610y.
[51] M.H. Habibi, H. Vosooghian, Photocatalytic degradation of some organic sulfides as environmental pollutants using titanium dioxide suspension, J. Photochem. Photobiol. Chem. 174 (1) (2005) 45–52, https://doi.org/10.1016/j.jphotochem.2005.02.012.
[52] C.R.S. de Oliveira, M.A. Batistella, A.A.U. de Souza, S.M. de, A.G. Ulson, And others, Synthesis of superacid sulfated TiO_2 prepared by sol-gel method and its use as a titania precursor in obtaining a kaolinite/TiO_2 nano-hybrid composite, Powder Technol. 381 (2021) 366–380, https://doi.org/10.1016/j.powtec.2020.11.063.
[53] W. Hajjaji, et al., Effective removal of anionic and cationic dyes by kaolinite and TiO_2/kaolinite composites, Clay Miner. 51 (1) (2016) 19–27, https://doi.org/10.1180/claymin.2016.051.1.02.
[54] K. Lazaar, et al., Efficiency of natural clay and titania P25 composites in the decolouring of methylene blue (MB) from aqueous solutions: dual adsorption and photocatalytic processes, Arabian J. Geosci. 14 (5) (2021) 1–10, https://doi.org/10.1007/s12517-021-06727-x.
[55] D. Kibanova, M. Trejo, H. Destaillats, J. Cervini-Silva, Photocatalytic activity of kaolinite, Catal. Commun. 12 (8) (2011) 698–702, https://doi.org/10.1016/j.catcom.2010.10.029.
[56] J. Hou, Y. Wang, J. Zhou, Y. Lu, Y. Liu, X. Lv, Photocatalytic degradation of methylene blue using a ZnO/TiO_2 heterojunction nanomesh electrode, Surf. Interfaces 22 (2011) 100889, https://doi.org/10.1016/j.surfin.2020.100889.
[57] L. Munguti, F. Dejene, Influence of annealing temperature on structural, optical and photocatalytic properties of ZnO-TiO_2 composites for application in dye removal in water, Nano-Struct. Nano-Obj. 24 (2020) 100594, https://doi.org/10.1016/j.nanoso.2020.100594.
[58] G. Sodeifian, R. Behnood, Application of microwave irradiation in preparation and characterization of CuO/Al_2O_3 nanocomposite for removing MB dye from aqueous solution, J. Photochem. Photobiol. Chem. 342 (2017) 25–34, https://doi.org/10.1016/j.jphotochem.2017.03.038.
[59] X. Li, H. Yang, Pd hybridizing ZnO/kaolinite nanocomposites: synthesis, microstructure, and enhanced photocatalytic property, Appl. Clay Sci. 100 (2014) 43–49.
[60] L.V. Barbosa, et al., Kaolinite-titanium oxide nanocomposites prepared via sol-gel as heterogeneous photocatalysts for dyes degradation, Catal. Today 246 (2015) 133–142, https://doi.org/10.1016/j.clay.2014.05.007.